# Identification of key liquid metal flow features in the physical conditioning of molten aluminium alloy with high shear processing

Mingming Tong[1,2], Jayesh B. Patel[3], Ian Stone[3], Zhongyun Fan[3], David J. Browne[1*]

1. School of Mechanical and Materials Engineering, University College Dublin, Ireland
2. Present address: Mechanical Engineering, NUI Galway, Ireland
3. BCAST, Brunel University, UK

* Corresponding author – david.browne@ucd.ie

## Abstract

Although treating molten alloy with high shear processing (HSP) can dramatically refine the microstructure of solidified aluminium alloys, it was also recently employed as part of an effective route to purification of contaminated aluminium alloy scrap. The key mechanisms of HSP include the dispersion of large aluminium oxide films and clusters into very fine oxide particles by the high shear rate, and the redistribution of bulk melt by the agitation. These fine oxides act as nucleation sites for iron-based intermetallic phases, the formation of which is a pre-cursor to purification of the alloy. Macroscopic flow features of HSP, such as flow rate and shear rate, influence its performance significantly. Simulation based on Computational Fluid Dynamics was used to predict key features of fluid flow during HSP in a static direct chill (DC) caster. It was found that the distribution of shear rate and mass flow rate is highly nonuniform in the caster, and only in the close vicinity of the mixing head is there a relatively high level of shear rate and effective melt agitation. Therefore, effective dispersion of oxide films and clusters, and resulting significant nucleation of the intermetallics and/or primary aluminium phase, can only occur near the mixing head, and not throughout the whole crucible. Confidence in the model validity was built, by comparison with post-solidification microstructures in a previous experiment with similar process parameters and geometry.

Keywords: rotor-stator mixer, high shear processing, computer simulation, shear rate, flow rate, aluminium alloy

## 1. Introduction

Treating liquid metal with high shear processing (HSP) has been found to have significant influence on the properties of solidified aluminium alloys and magnesium alloys. As reviewed by Fan and co-workers [1,2], shearing the molten alloy in the liquid state using a rotor-stator mixer can dramatically refine the microstructure of direct chill (DC) cast aluminium alloys. Specifically, the HSP process can produce very fine equiaxed dendrites in the cast alloy [3] without using grain refiners. The high shear rate generated by the closed coupled rotor-stator mixer effectively fragments large aluminium oxide films and clusters into fine individual particles [4]. In high grade aluminium alloys, in which the content of iron and manganese is relatively low, the oxide particles were found to have very low lattice misfit with the α-Al phase on close packed crystallographic planes [5]. On cooling liquid aluminium alloys that have a relatively high level of iron (e.g. 1 wt% or higher), the iron-bearing intermetallics normally precipitate before the appearance of α-Al phase [6]. The lattice misfit between the aluminium oxide and iron bearing intermetallics was also found to be very low [7]. Therefore, the fine oxide particles act as potent nucleation sites for both the intermetallic and α-Al phases [8,9], during the solidification of aluminium alloys, and hence refine the microstructure of corresponding cast samples. Haghayeghi and Nastac have also reported [10] that shearing of a molten aluminium alloy prior to solidification resulted in a finer equiaxed grain size.

Besides the influence on microstructure refinement, it has recently been realized that HSP has great potential in purifying contaminated aluminium alloys. Iron is a very common and usually detrimental impurity in recycled aluminium alloys. An excessive level of iron can dramatically reduce the mechanical properties of the cast products. Due to the related thermodynamic features of such alloys [6,8], iron-bearing intermetallics (e.g. α AlFeMnSi) can effectively collect the iron component from molten scrap alloy while the primary α-Al solid solution phase is not yet formed [11]. Because the solid intermetallics are denser than the rest of the molten alloy, they can be separated from the bulk material by using a sedimentation technique, and hence the level of iron in the treated material is decreased. Such physical conditioning of the molten alloy using HSP is being used as the major technique in research on alloy purification, whereby the authors are trying to manufacture high performance aluminium alloys by processing contaminated recycled aluminium scrap.

With the purpose of purifying the contaminated material, the key factor of HSP is the shear of molten metal by the rotor-stator mixer. The nucleation of iron-bearing intermetallics or primary α-Al phase is only effective when there is large number of available potent nucleation sites present. As presented in previous work [12], the shear rate was found to have a dominant influence on the breakage of oxide clusters during HSP. In order to systematically understand the influence of HSP process parameters on the resultant size of oxides, the flow features of the liquid metal (including particularly the shear rate and flow rate of melt) during the HSP with rotor-stator mixer have to be characterised.

Although there are a variety of experimental methods that are capable of measuring the features of fluid flow, such as Laser Doppler Anemometry and Particle Image Velocimetry, they are very difficult to apply in the measurement of flow features inside an opaque liquid metal. Because the molten metal is non-transparent, at high temperature and maybe flammable (e.g. magnesium alloys), it is infeasible or dangerous to place such experimental measurement equipment very close to the liquid that is being treated by HSP when operating the mixer. Therefore, computer modelling and simulation provide a very good alternative to calculate the related key features of melt flow during HSP.

Using computational fluid dynamics (CFD), computer simulation has been extensively employed in the prediction of flow features of metal processing, including such as casting [13] and welding [14,15]. In comparison, CFD modelling of melt conditioning is relatively rare. The majority of this has been dedicated to the degassing processes taking place in the gas stirred ladle of liquid metals [16-18]. CFD modelling has been applied to precipitation processes occurring in a mechanically agitated tank [19], in which a standard combination of baffle and impeller is used to agitate the fluid. However, the rotor-stator mixer that is used in HSP is such a closely coupled device [1,20] that it is inherently different from such a baffle-impeller combination. The published CFD modelling that is most relevant to the HSP process of our interest is the work by Utomoa et al. [21, 22], in which a variety of flow features were analysed in the 3D CFD modelling of treating water with a rotor-stator mixer [21, 22]. However, respective results were only analysed along the radius of the mixer and there were no analyses of flow features through the depth of the tank. Moreover, the rotor-stator mixer that was employed in the research of [21,22] is a type of commercially available mixer with major applications in food, cosmetics, chemical and pharmaceutical industries. The novel rotor-stator mixer that is employed in the HSP of liquid metal [1,20] is a recently invented

device. Its design is very different from that of the conventional mixer (e.g. those used in [21,22]). Taking the dramatic differences between the properties of liquid metal (e.g. liquid aluminium alloy) and those of water into account (e.g. in terms Weber number and Prandtl number), we have had to develop a new CFD model in order to understand and predict the flow features of interest in the case of treating liquid metal with HSP.

In this paper, we firstly specify the configuration of the experimental device and computational case study. Then we present the details of our computational model and computer software. The key features of fluid flow simulations are analysed. Key computational predictions are compared with available experimental results from an HSP-treated solidified ingot, in order to provide confidence in the model.

## 2. Configuration of the case study and CFD model

The detailed configuration of treating liquid metal with HSP by using rotor-stator mixer can be found in the Fig.1 of [23]. Figure 1a of the current paper schematically illustrates the overall setup of HSP of liquid metal, and Fig.1b specifies some key dimensions of the mixing head, the 3D shape of which can be seen in Fig. 2. In the crucible (or mould), the impeller operates at relatively high speed. At the side of the stator near the mixing head, there are rows of small holes, numbered as shown in Fig. 1b. At the bottom of the mixing head, there is a relatively large opening. The liquid metal can flow in and out of the mixing head through these holes and opening.

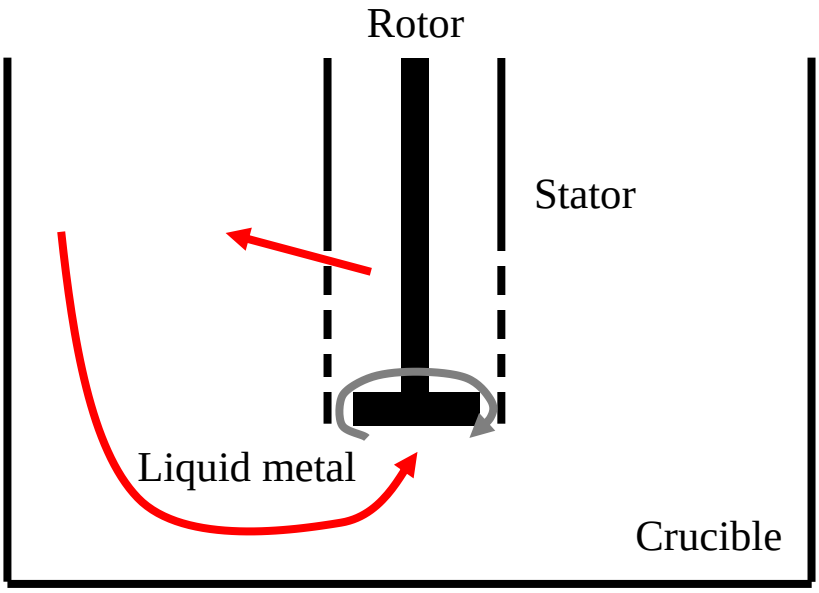

(a)

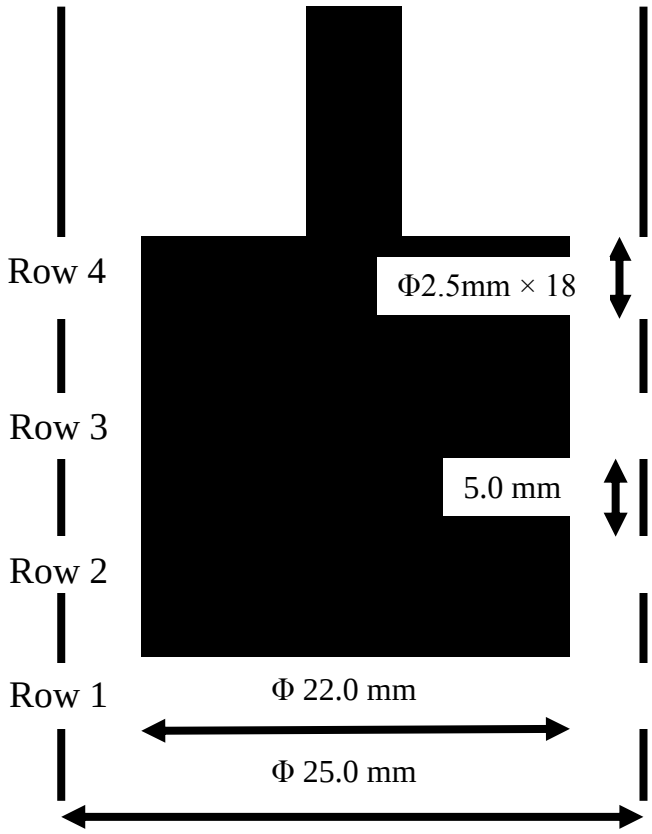


(b)

Fig.1. Configuration of HSP process including the (a) overall setup, and (b) key dimensions of the mixing head

The static DC caster is a cylindrical container of 60 mm in diameter. It is filled with liquid AA6060 aluminium alloy, to a depth of 120 mm. The rest of the caster contains air, above the liquid metal. The intent is to model the experiment carried out by Jones at al. [23], in which the mixer was removed from the superheated melt prior to alloy solidification. The mixer consists of a high speed spinning rotor and a stationary stator, which are coaxial and separated by a very small gap. The rotor consists of a long shaft with an impeller at its end, having four flat blades. The stator is a hollow tube, near the end of which is a series of circular holes in the wall. The geometry of the head of the mixer (i.e. the mixing head) can be seen in Fig.1. As stated, the specific 3D geometrical features of the mixing head are

illustrated in Fig.2. The outer and inner diameters of the stator are 25 mm and 22 mm, respectively, and the diameter of the impeller is 21.5 mm. The rotor-stator annular gap is therefore 0.25mm. There are 72 radial holes of 2.5 mm diameter in the stator, which are aligned along four rows or rings (of 18 equally spaced holes each). The impeller blades are 19 mm long. The mixer is placed inside the static DC caster at a depth of 70 mm relative to the bottom of the mixing head. The impeller speed is 4000 rpm.

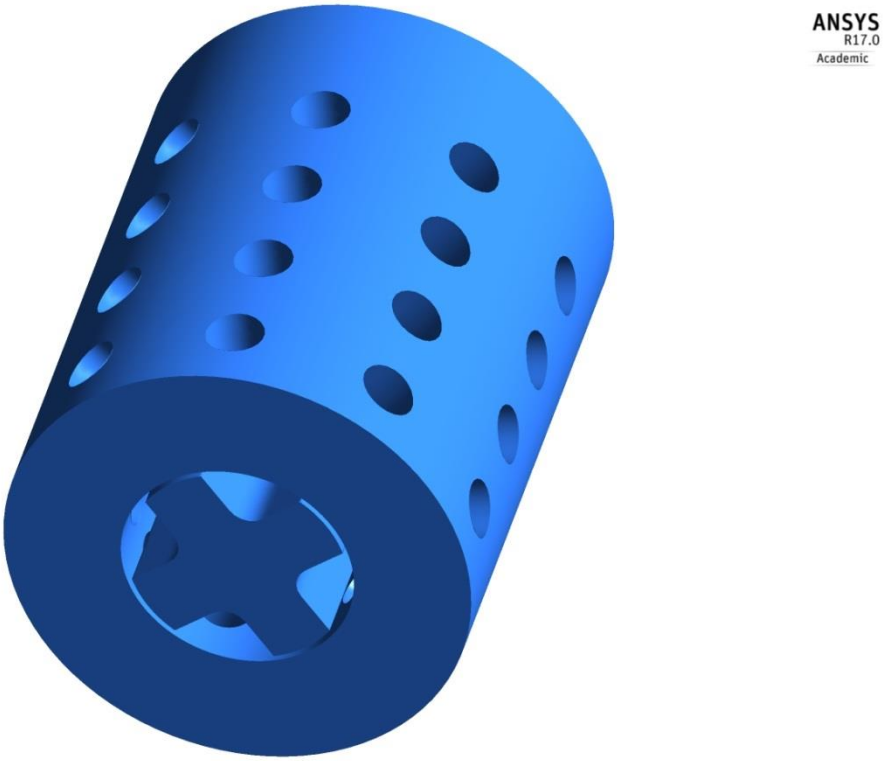


Fig.2. 3D geometrical features of the mixing head

The overall fluid flow problem is mathematically formulated with the conservation equations of mass and momentum, in 3D Cartesian coordinates:

$$\frac{\partial \rho}{\partial t} + \nabla \cdot (\rho \vec{V}) = 0, \qquad (1)$$

$$\frac{\partial \rho \vec{V}}{\partial t} + \nabla \cdot (\rho \vec{V} \vec{V}) = -\nabla p + \nabla \cdot \bar{\bar{\tau}} + \vec{F}, \qquad (2)$$

where $\rho$ is the density, $t$ time, $\vec{V}$ velocity, $\overline{\overline{\tau}}$ stress, $p$ pressure and $\vec{F}$ the body force. The turbulence feature of fluid flow is taken into account by using the Realizable $k-\varepsilon$ model [24]:

$$\frac{\partial(\rho k)}{\partial t}+\nabla\cdot(\rho k\vec{V})=\nabla\cdot[(\mu+\frac{\mu_t}{\sigma_k})\nabla k]+G_k-\rho\varepsilon, \tag{3}$$

$$\frac{\partial(\rho \varepsilon)}{\partial t}+\nabla\cdot(\rho \varepsilon\vec{V})=\nabla\cdot[(\mu+\frac{\mu_t}{\sigma_\varepsilon})\nabla \varepsilon]+C_l\rho E\varepsilon-\rho C_2\frac{\varepsilon^2}{k+\sqrt{\nu\varepsilon}}, \tag{4}$$

$$\mu_t=C_u\rho\frac{k^2}{\varepsilon}, \tag{5}$$

where $k$ is the turbulence kinetic energy, $\varepsilon$ the turbulent dissipation rate and $\mu_t$ the turbulent viscosity. The rest of the parameters are all in connection with the features of turbulence and can be found in [24]. In order to properly formulate the fluid flow near the rigid walls, the enhanced wall treatment [25] is employed here. It is valid to formulate the fluid flow features throughout the whole near-wall region (including the viscous sublayer, buffer region, and log-law region), across which the fluid flow can vary from fully laminar to fully turbulent. The interface between the liquid metal and air is implicitly captured by the volume of fluid (VOF) method [26]:

$$\frac{\partial(\alpha_i)}{\partial t}+\nabla\cdot(\alpha_i\vec{V}_i)=0, \tag{5}$$

where $\alpha$ is the volume fraction of the phase $i$ in a control volume. By determining the volume fraction of all the phases (*i=1,2 in the liquid-gas two phase system of this paper)* in the control volumes using the transport equation of Eq.5, the scalar properties of control volumes that resolve the liquid-gas interface can be determined by using appropriate method of averaging (e.g. mass weighted average with regard to density). Therefore, only a single momentum equation (Eq.2) and a single continuity equation (Eq.1) have to be solved, which makes this method of two-phase fluid flow simulation computationally economical. In the computational results, all the variables (such as pressure and velocity etc.) are shared by all the phases. When calculating the flux of parameters of interest at the walls of the control volumes that represent the liquid-gas interface, the geometric reconstruction method [27] is

used, which reconstructs the interface between fluids using a piecewise-linear approach based on the value and derivatives of the volume fraction $\alpha$.

In the computation, the surface of the rotor, stator and static DC caster are all assumed to be rigid walls, at which the non-slip boundary condition of the fluids is assumed. The surface tension at the liquid-air interface is formulated by using the continuum surface force model [28], which maps the surface force onto the control volumes that are near the liquid-air interface.

The rotor spins at high speed and it strongly agitates the fluid. The sliding mesh method [29] is employed in order to take the rotational movement of the impeller and its influence on the fluid flow into account. When applying the sliding mesh method, the mesh of fluid(s) zone is partitioned into multiple subzones, which share non-conformal interfaces. As the rigid walls of the rotor move, the corresponding subzones of the fluid (e.g. the fluid subzone that closely surrounds the rotor) correspondingly move in a rigid way (i.e. there is no deformation of the mesh). This method is believed to be a better method for formulating the model of fluid agitation by the close coupled rotor-stator mixer than the alternative method that moves the reference frame.

The overall simulation domain is discretized with tetrahedral mesh of adaptive resolution, in order to resolve the geometrical features of different sizes at different places of the domain. The mesh size varies between around 0.1 mm and 5 mm. The overall governing equations are solved with the SIMPLE method [30], in order to find the transient solution of the target problem. The size of the time step is $5\times10^{-4}$s. The computation was implemented by using the FLUENT module of ANSYS, and the details of the related mathematical models and computation can be found in [29]. In the computation, the value of density and dynamic viscosity of the liquid aluminium alloy and the surface tension coefficient of the melt-air interface was employed as 2700 kg/m$^3$[31], 0.0027 Pa·s [32] and 0.87 N/s [33]respectively.

## 3. Simulation results

### 3.1 Net mass flow rate through the mixing head

We firstly analyzed the temporal evolution of the mass flow rate of the liquid metal through the stator holes; Fig. 2. As can be seen from Fig.1, there are four rows of holes at the side of the stator. The mass flow rates through the various rows are different. The mass flow rate through the first row of holes, near the bottom of the mixing head, is relatively low in magnitude and has a negative sign. This means that the liquid metal is actually flowing into the mixing head through this row of holes. The rate of melt flow through the second and fourth rows of holes is comparatively higher, and flowing out of the mixing head. The flow rate through the third row of holes of the stator is the greatest. Summing the mass flow rate through all four rows of stator holes, we find the net mass flow rate of the liquid metal flowing out of the mixing head. In Fig.3, we see that the total net mass flow rate through the mixing head reaches a plateau value of 0.12 kg/s after 0.71 s of shearing. In the following part of this section, we analyze related flow features of the liquid metal at this moment of 0.71 s of shearing.

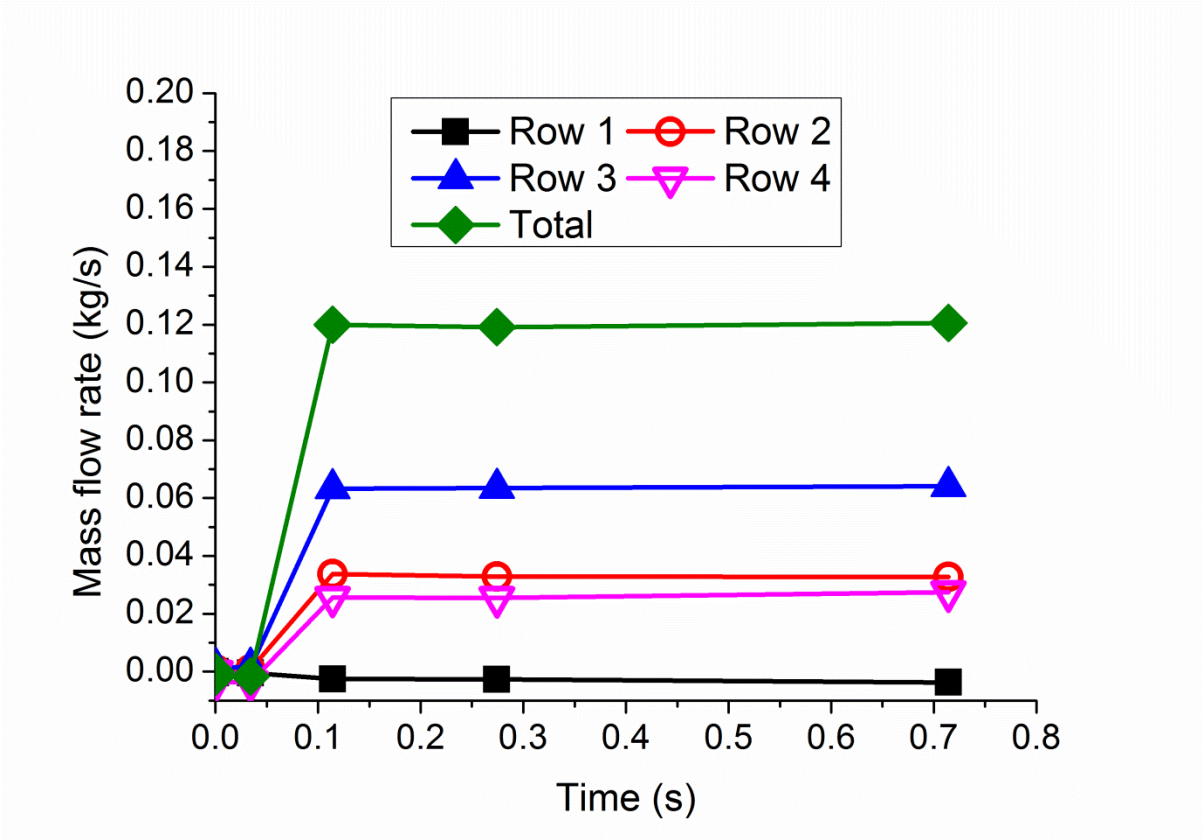


Fig.3. Temporal evolution of the mass flow rate of the liquid metal flowing through the mixing head

3.2 Flow pattern inside the mixing head

In order to analyze the flow pattern inside the mixing head, we sample the velocity of liquid metal along a virtual interface of revolution in parallel to the shaft of the impeller of 16 mm in diameter, as shown by the vectors in Fig.4. It can be seen that the liquid metal flows upwards into the mixing head from its bottom near the root of the impeller blades. This upward flowing stream of liquid metal quickly changes its direction from axial to circumferential. While sampling the velocity of fluid flow along a central plane through the rotor shaft which bisects two facing columns of holes, as shown in Fig.5, it can be seen that there is a very weak recirculation of the liquid metal inside the mixing head along its length which is accompanied by the outward flow of the liquid metal through the holes of the stator at its side.

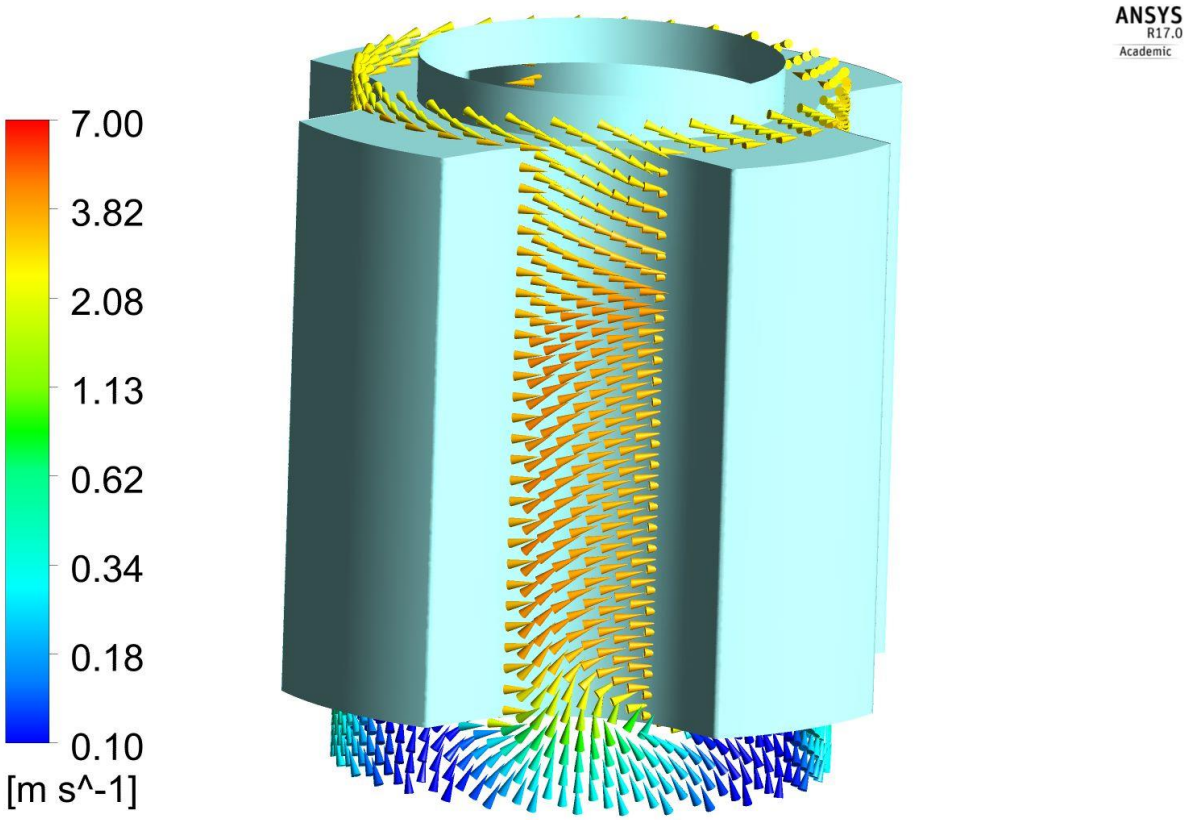


Fig.4. Velocity vectors of the liquid metal along a surface of revolution of 16 mm in diameter, parallel to the shaft of the impeller, at 0.71 s.

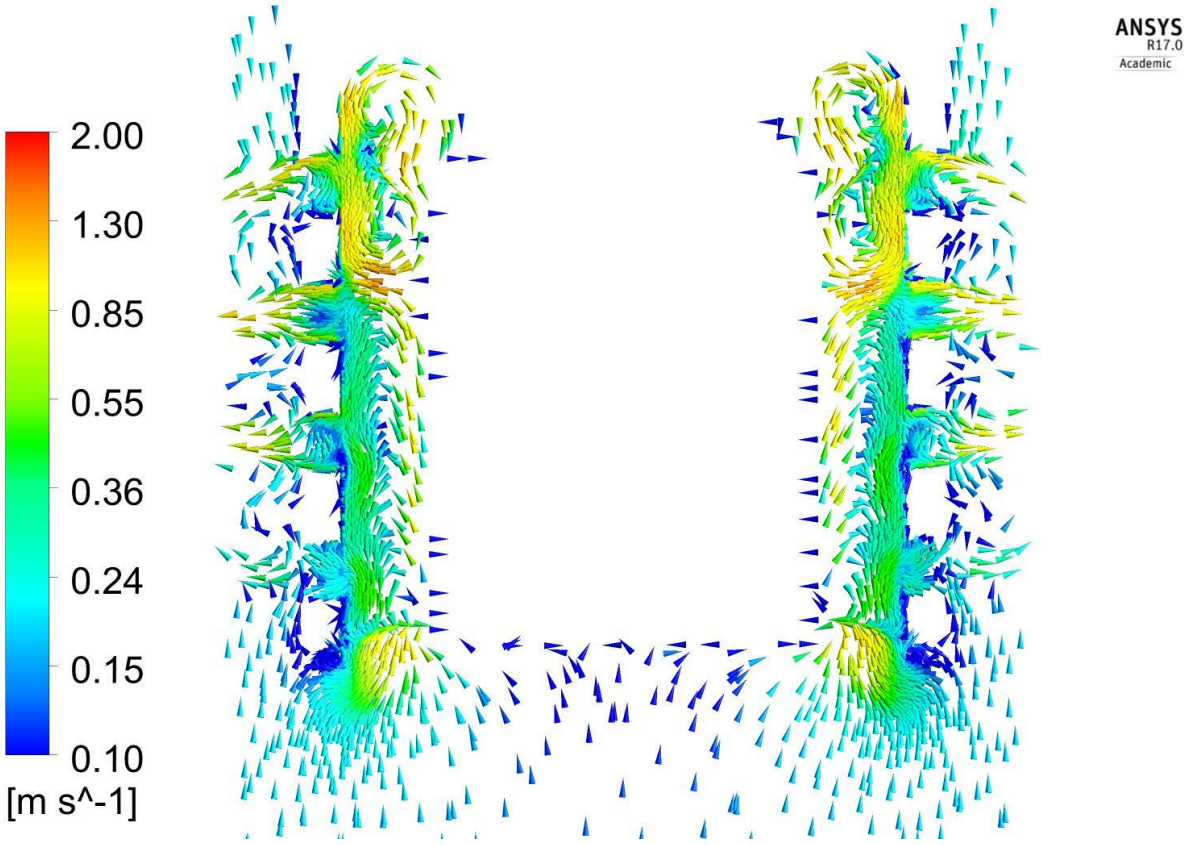


Fig.5. Velocity vectors of the liquid metal projected to a plane that is along the center of the rotor shaft around the mixing head, at time 0.71 s of shearing

The pressure field inside the mixing head, as shown in Fig.6, caused such a melt flow pattern inside the mixing head. Due to interactions between the flowing liquid metal, the moving impeller and the stationary stator, a high pressure zone occurs near the internal surface of the mixing head around the third row of holes. This high pressure zone creates an outward pressure gradient, which drives the liquid metal out of the mixing head. At the same time, due to the centrifugal force, a low pressure zone occurs near the root of the impeller blades around the bottom of the mixing head. This low pressure zone sucks the liquid metal into the mixing head from below. Near the large opening at the bottom of the mixing head, the low pressure zone extensively expands from the root of impeller blades towards the internal orifice of the first row of holes of the stator at its side. Therefore, the liquid metal is actually flowing into the mixing at a very low rate through the holes of the first row, instead of flowing out.

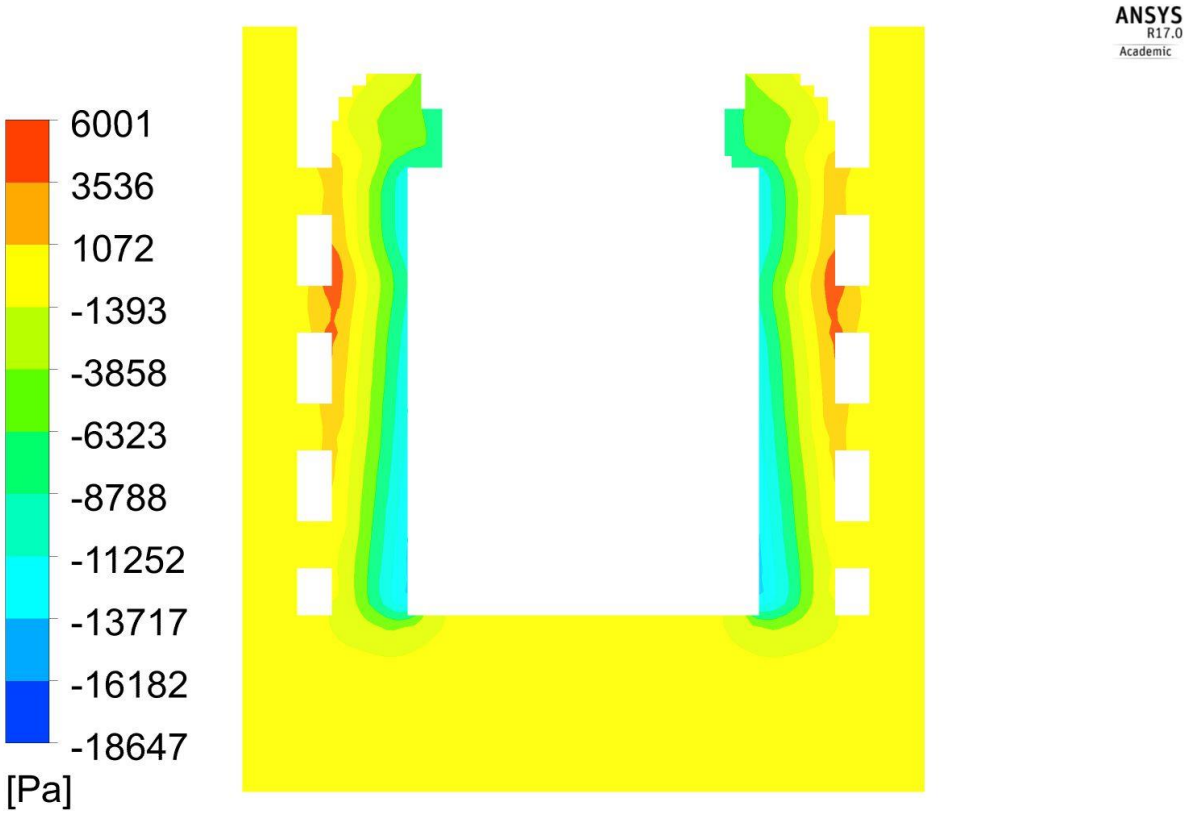


Fig.6. Contour of pressure at a plane that is along the centre of the shaft rotor, at 0.71 s.

3.3. Fluid agitation in the overall caster

In order to characterise how well the bulk liquid metal is agitated, we zoom out to the scale of the overall caster. Figure 7 illustrates the melt flow field in a central plane that is along the shaft of the rotor. The model predicted that, while the liquid melt is flowing at a very high speed inside the mixing head, it is very quickly and dramatically decelerated as soon as it shoots out of the mixing head through the stator holes. Because the circumferential and axial profile of the magnitude of the melt velocity is highly non-uniform, we sampled the maximum melt velocity along virtual surfaces of revolution, 20 mm high (starting from the bottom of the mixing head upwards), and of different diameters, near the mixing head and parallel to the shaft of the rotor, and used it as the representative velocity of the melt jets that shoot out of the mixing head. As shown in Fig.8, the velocity of melt jets evolves from around 5.1 m/s down to around 1.2 m/s while shooting out of the mixing head. Within a distance of 10 mm outside the stator (between the radial position of 15 mm and 25 mm

relative to the shaft), the melt velocity decreases from 1.2 m/s to 0.4 m/s. Such dramatic deceleration is due to the fact that the momentum of the outshooting liquid metal jets is comparatively low, since the diameter of the holes at the side of the stator is very small compared with the diameter and depth of the overall caster. Therefore, the velocity of the melt jets is very quickly dissipated by the comparatively stagnant bulk liquid metal of the overall caster, due to conservation of momentum. The comparatively high viscosity of liquid metal also contributes to the damping of the velocity of the outshooting liquid metal jets.

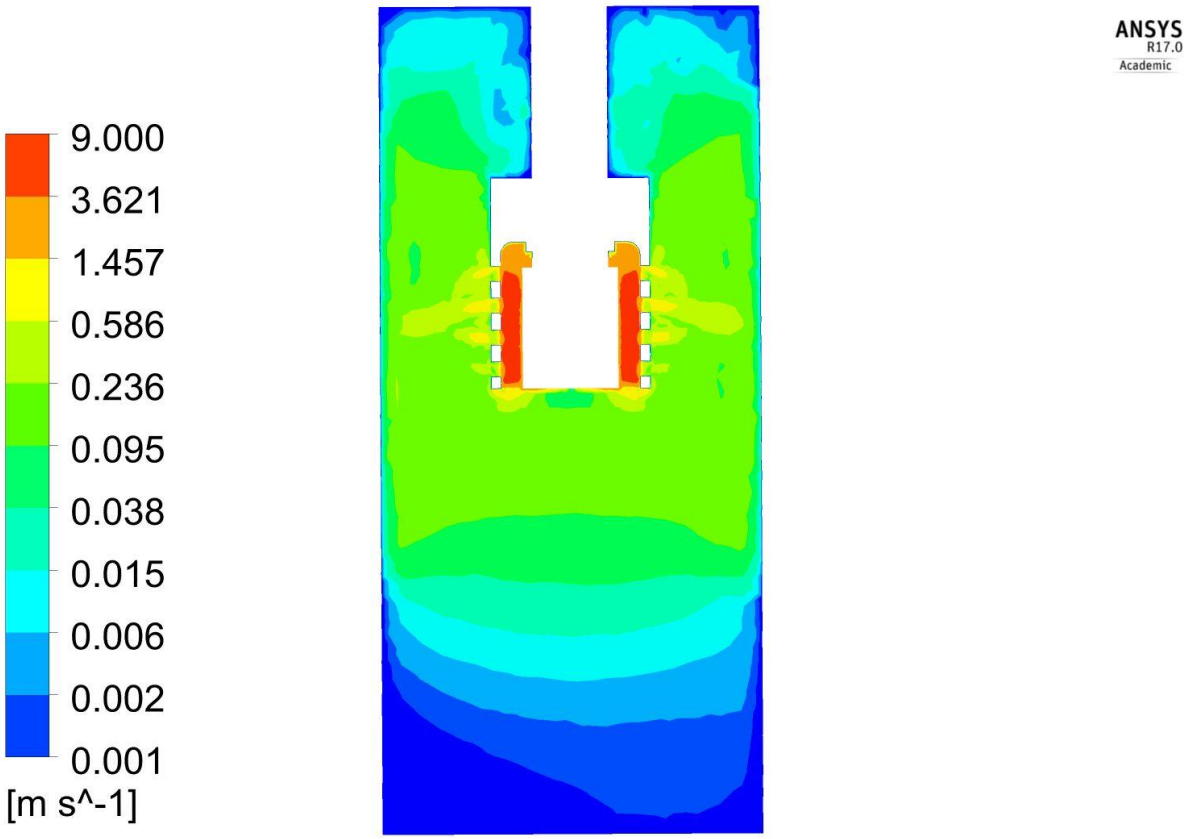


Fig.7. Contour of the magnitude of the velocity of liquid metal at a central plane, at 0.71 s.

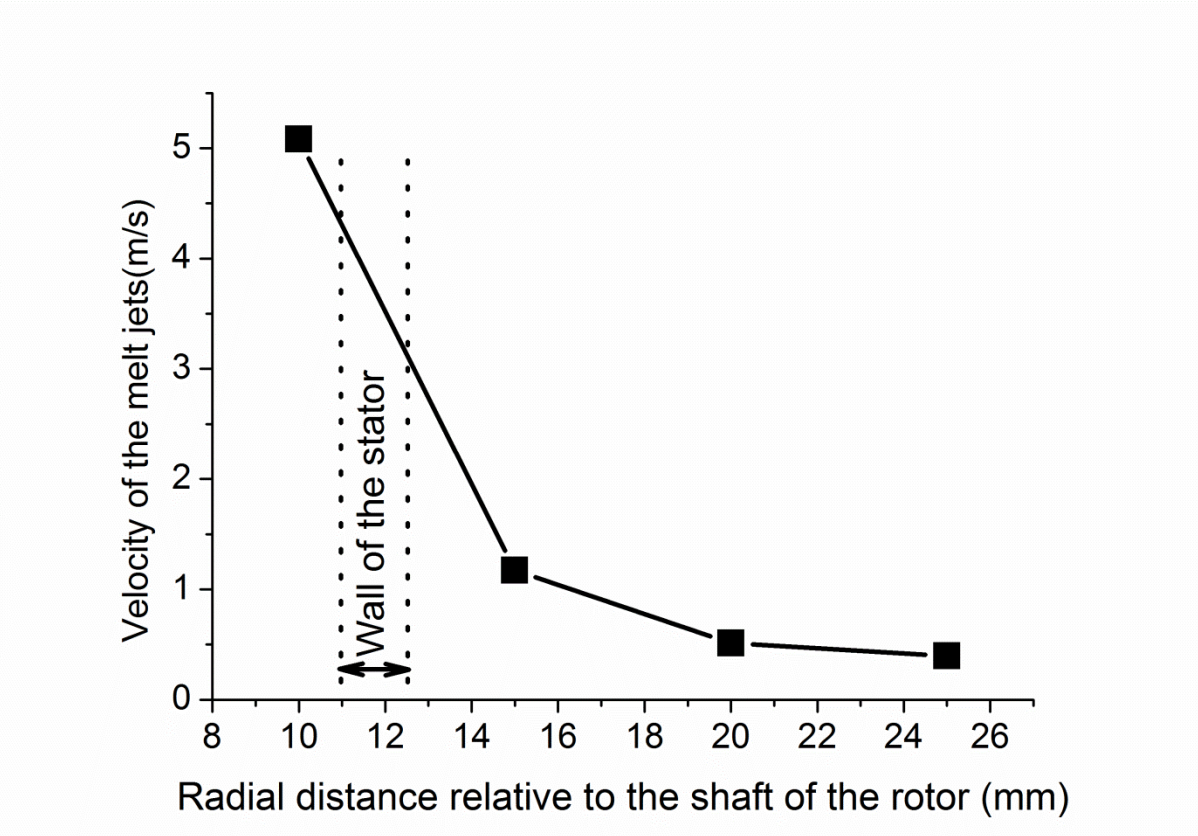


Fig.8. Radial profile of the maximum magnitude of the melt velocity in the close vicinity of the mixing head, at 0.71 s.

Analysis of the stream lines of fluid flow, as shown in Fig.9, shows how the liquid metal is redistributed throughout the overall caster. In the close vicinity of the mixing head, there are two strong counter-rotating recirculations of the liquid metal above and below the third row of stator holes. The melt recirculation above the third row of holes is so localized and strong that the bulk liquid metal above the third row of the holes of the stator has very little chance to flow into the mixing head. The melt recirculation below row 3 entrains some bulk liquid metal into the mixing head, mainly through the large opening at the bottom of the mixing head, and is sheared. Below the mixing head, the melt flows at relatively low velocity, particularly near the bottom of the caster. Comparing Fig.9 with Fig.8, we conclude that only the melt in the close vicinity of the mixing head is well agitated by the mixer, and only that part below the third row of stator holes has a good chance to be redistributed via the mixing head.

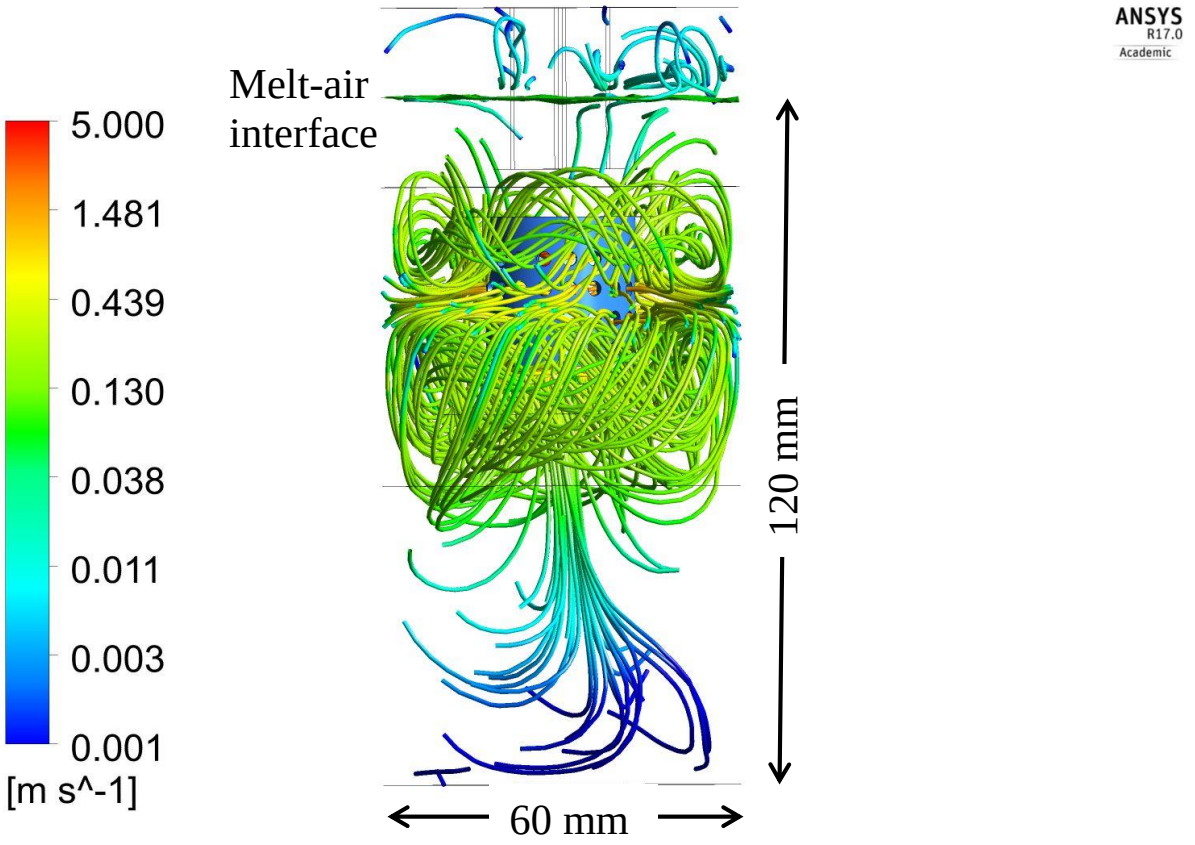


Fig.9. Stream lines of fluid flow, at the time of 0.71 s.

3.4. Shear rate

Shear is a very important phenomenon in HSP. The liquid shear rate is responsible for the dynamics of agglomeration and breakage of the dispersed phases. Before calculating the value of shear rate, we have to firstly determine if the fluid flow is laminar or turbulent. When the fluid flow is laminar, the shear rate is the gradient of the velocity of fluid (assuming the fluid is incompressible). When the fluid flow is turbulent, shear rate is a function of the turbulence dissipation rate as:

$$\sigma = \sqrt{\frac{\varepsilon}{\nu}}, \tag{6}$$

where $\sigma$ is the characteristic shear rate, $\varepsilon$ is the turbulence dissipation rate, and $\nu$ is the kinematic viscosity of the melt. As shown in Fig.10, in the overall caster, the value of viscosity ratio (ratio of the turbulent viscosity to the physical viscosity) is mostly above 20. This means that the fluid flow in the whole caster falls in the regime of turbulent flow.

Therefore, we use the turbulence dissipation rate and Eq.6 when computing the shear rate of the melt.

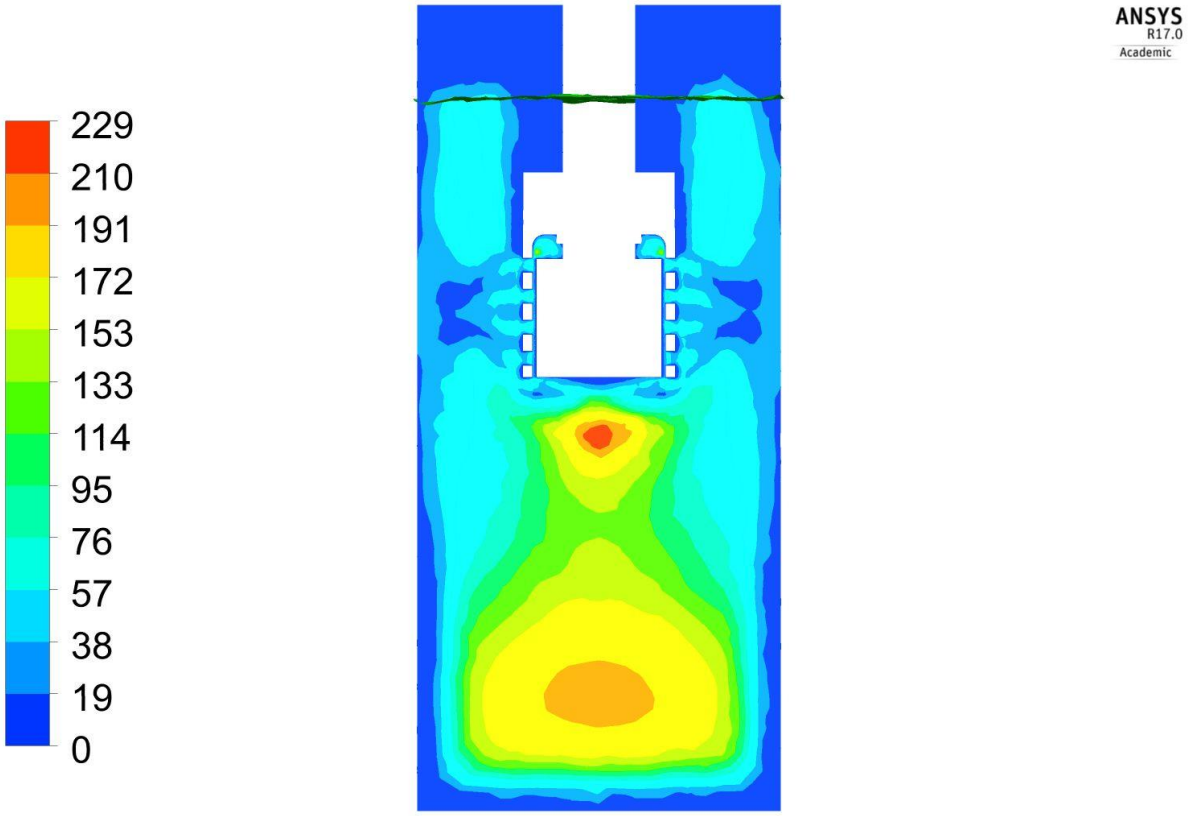


Fig.10. Contours of turbulent viscosity ratio at a central plane through the shaft of the rotor, at 0.71 s.

The contours of turbulence dissipation rate that are shown in Fig.11 illustrate that values of turbulence dissipation rate are relatively high in the close vicinity of the mixing head (and particularly between the rotor and the stator) and the value in the far field of the bulk melt is relatively low. This means that we can only expect high level of shear rate in the close vicinity of the mixing head.

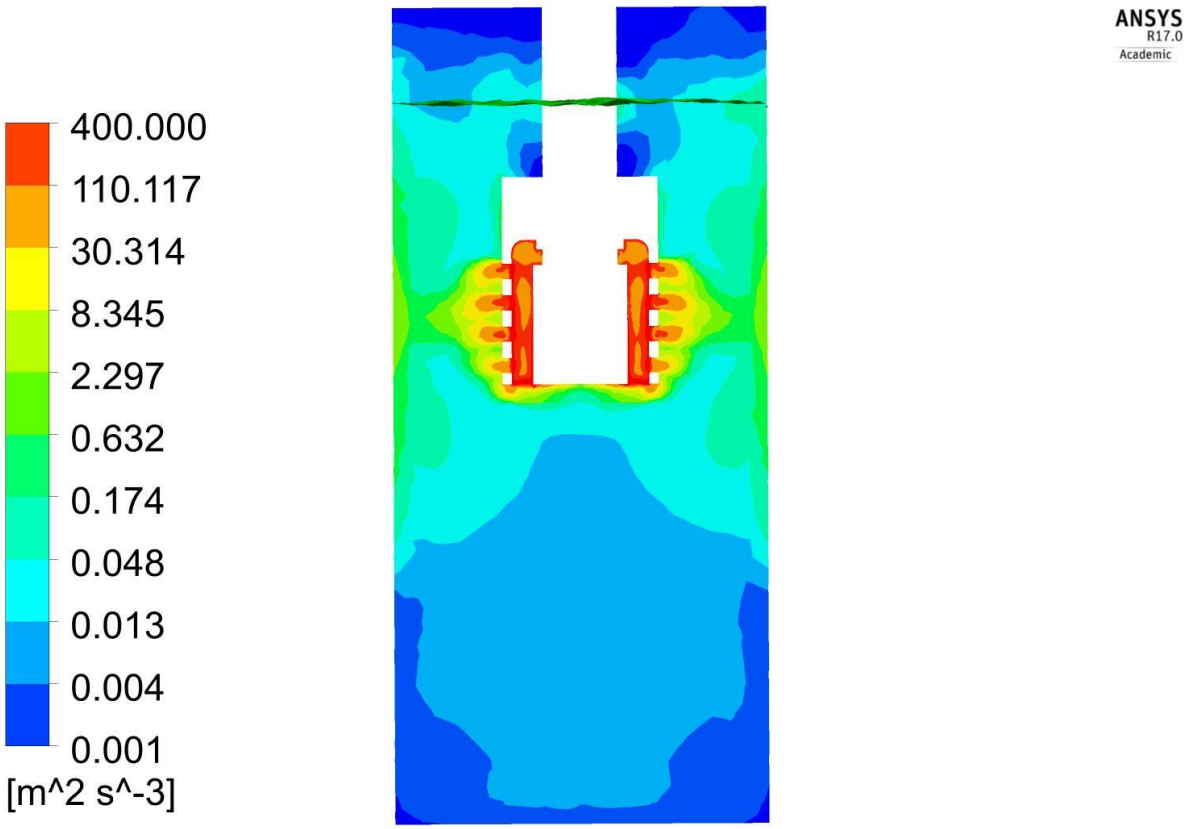


Fig.11. Contours of turbulence dissipation rate at a central plane along the shaft of the rotor, at 0.71 s.

If we sample the value of turbulence dissipation rate on a plane that is normal to the shaft of rotor along the third row of stator holes, as shown in Fig.12, we can clearly see its radial and circumferential profile. Inside the mixing head (particularly inside the gap between the rotor and the stator and inside the stator holes), the level of the turbulence dissipation rate is relatively high. Outside the mixing head however, the level is quite low. Along the circumference of the mixing head, the circumferential profile of the turbulence dissipation rate follows the geometrical features of the stator (i.e. size and spacing of the holes in its wall) and the rotor (i.e. size and number of blades).

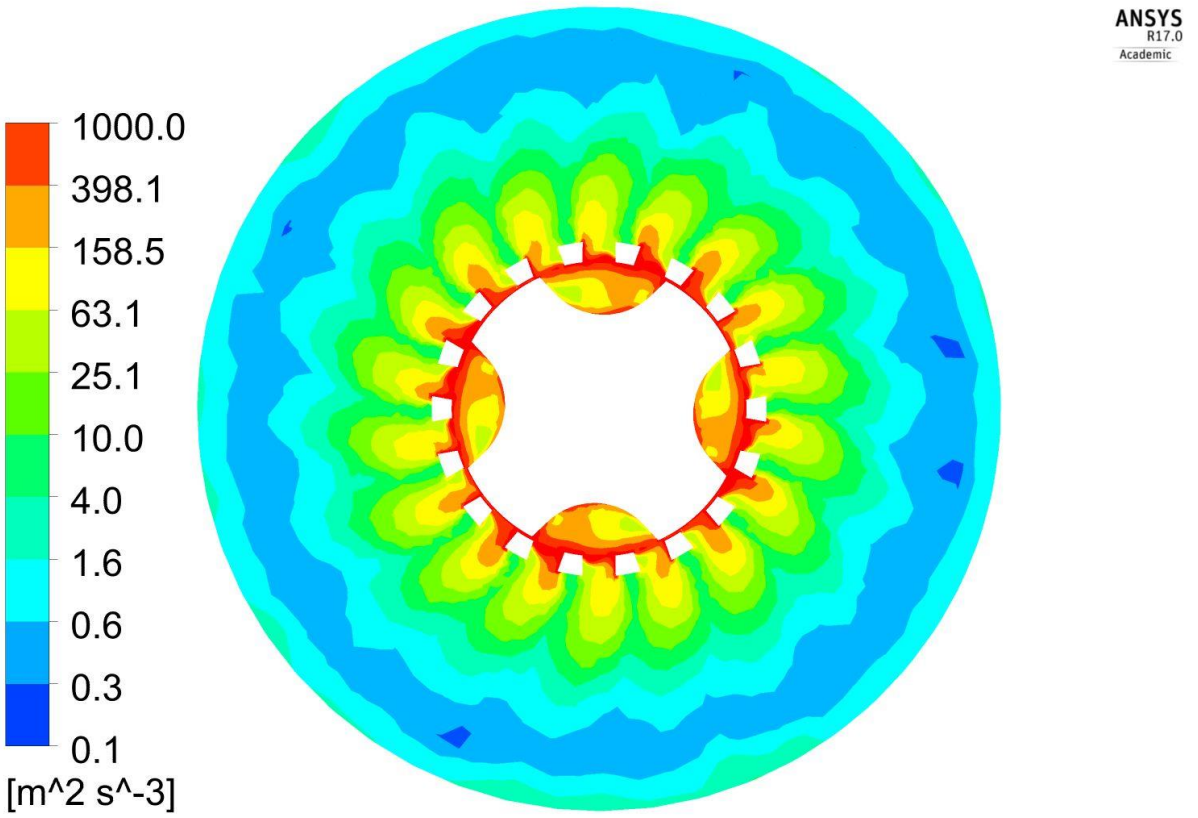


Fig.12. Contour of the turbulence dissipation rate at a plane normal to the shaft of the rotor, at row 3 of stator holes, at 0.71 s.

Quantitatively, we computed the maximum value of the characteristic shear rate at different virtual surfaces of revolution, again 20 mm high (starting from the bottom of the mixing head upwards), and of different diameters, parallel to the shaft of the rotor around the mixing head, and used it as the representative shear rate as a function of the radial position of the melt as shown in Fig.13. We can see that the shear rate has the highest value of $1.11\times10^{5}$ $s^{-1}$ inside the mixing head (radial position of 10 mm). The value of the shear rate decreases by around an order of magnitude (down to $1.14\times10^{4}$ $s^{-1}$) as the melt flows out of the holes of the stator (i.e up to radial position of 15 mm). As the melt flows near the wall of the caster (radial position of 25 mm), the value of shear rate further decreases by another order of magnitude (down to 960 $s^{-1}$). The results shown in Fig.13 show that, due to the closed coupled feature of the rotor-stator mixer, there is a high level of shear rate only inside the mixing head; elsewhere the shear rate is relatively low.

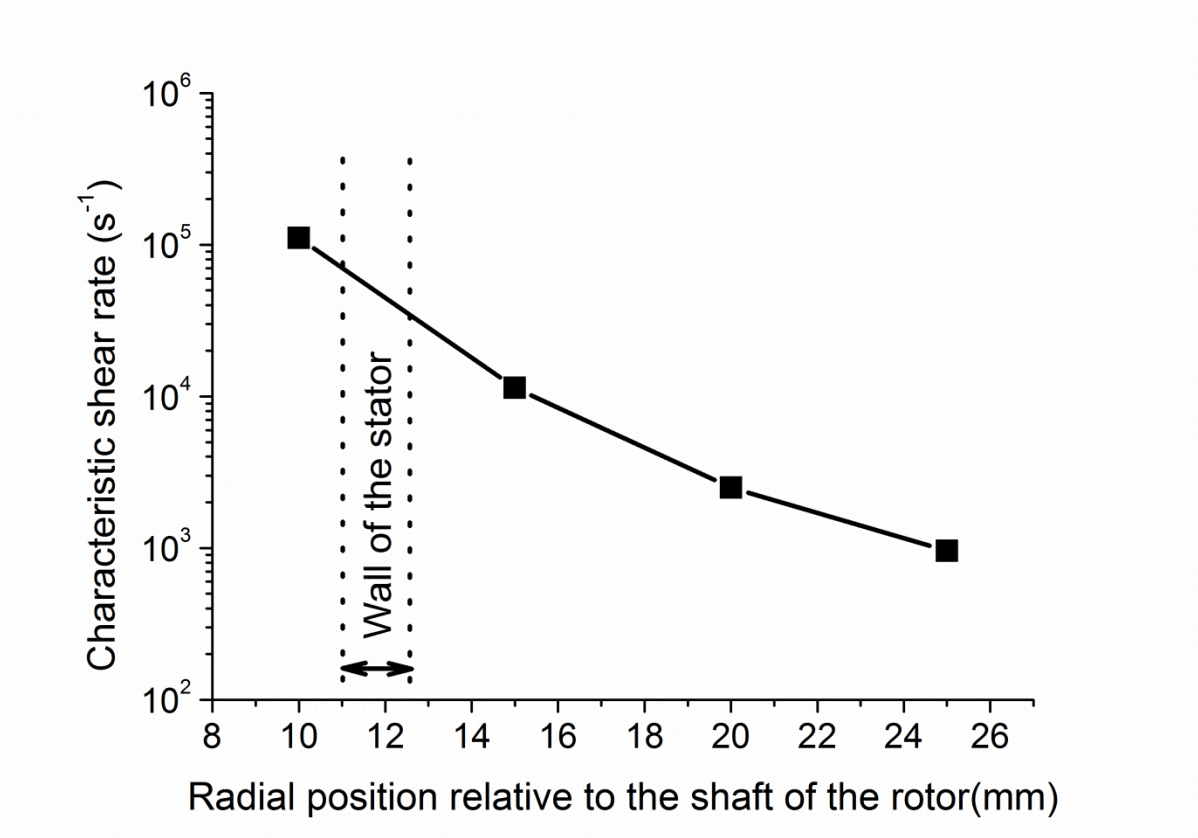


Fig.13. Radial profile of the maximum characteristic shear rate at 0.71 s.

3.5 Experimental validation

In the experimental research of Jones et.al. [23], HSP was employed in the treatment of molten AA6060 alloy in a static DC caster. The process parameters that were employed in the presented computer simulation were chosen to agree well with those that were used in the previous experiments [23] on commercially pure aluminium (alloy AA 60060). So the modelling results are directly relevant to those experimental findings.

The microstructure of the solidified alloy billet was characterised with optical metallography, and dramatic variation of the microstructure was found along the height of the billet. As shown in Fig.14, near the bottom of the billet, the dendrites are coarse columnar dendrites parallel to the billet axis, which is followed by a second zone of columnar dendrites that tilt at an angle to the lower ones. Above the second zone of columnar dendrite, there is a zone of very refined equiaxed dendrites. Above the fine equiaxed dendrite zone, there is a second

zone of coarser equiaxed dendrites. Jones et.al. [23] deduced qualitatively that it was the influence of melt flow features that caused such variation of microstructure along the height of the solidified billet, due to oxide fragmentation caused by melt shear. These oxides act as nucleating agents for Fe-based intermetallics and then primary aluminium. They placed the mixing device at a similar depth as that used in our simulations, switched it on and removed it from the crucible whilst the melt was still superheated.

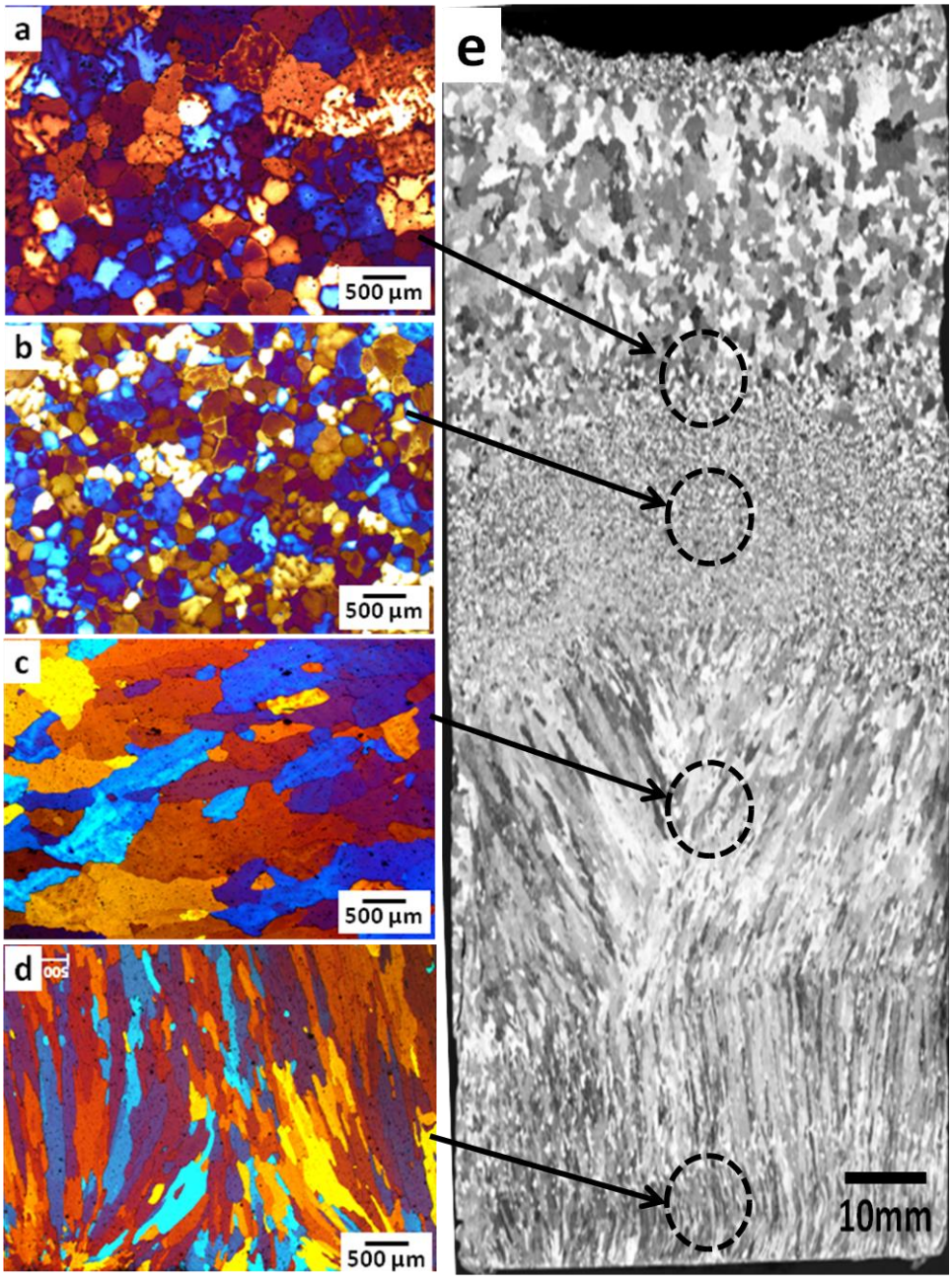


Fig.14. Microstructure of the solidified AA6060 billet (reproduction of Fig.5 of [23]).

In order to quantitatively analyze the possible influence of melt flow features on the microstructure of the solidified billet via our computational model, when analysing the simulation results, we section the height of the melt with several virtual planes that are normal to the height of the caster. The maximum value of the characteristic shear rate and the area-averaged absolute value of the component of the melt velocity that is normal to these virtual planes are sampled. In the meanwhile the grain size was experimentally measured at the representative positions shown in Fig. 14 (a-d). The variation of the maximum shear rate, average absolute velocity of the melt along the depth, and grain size of the solidified billet are illustrated in Fig.15 as a function of height relative to the bottom of the caster.

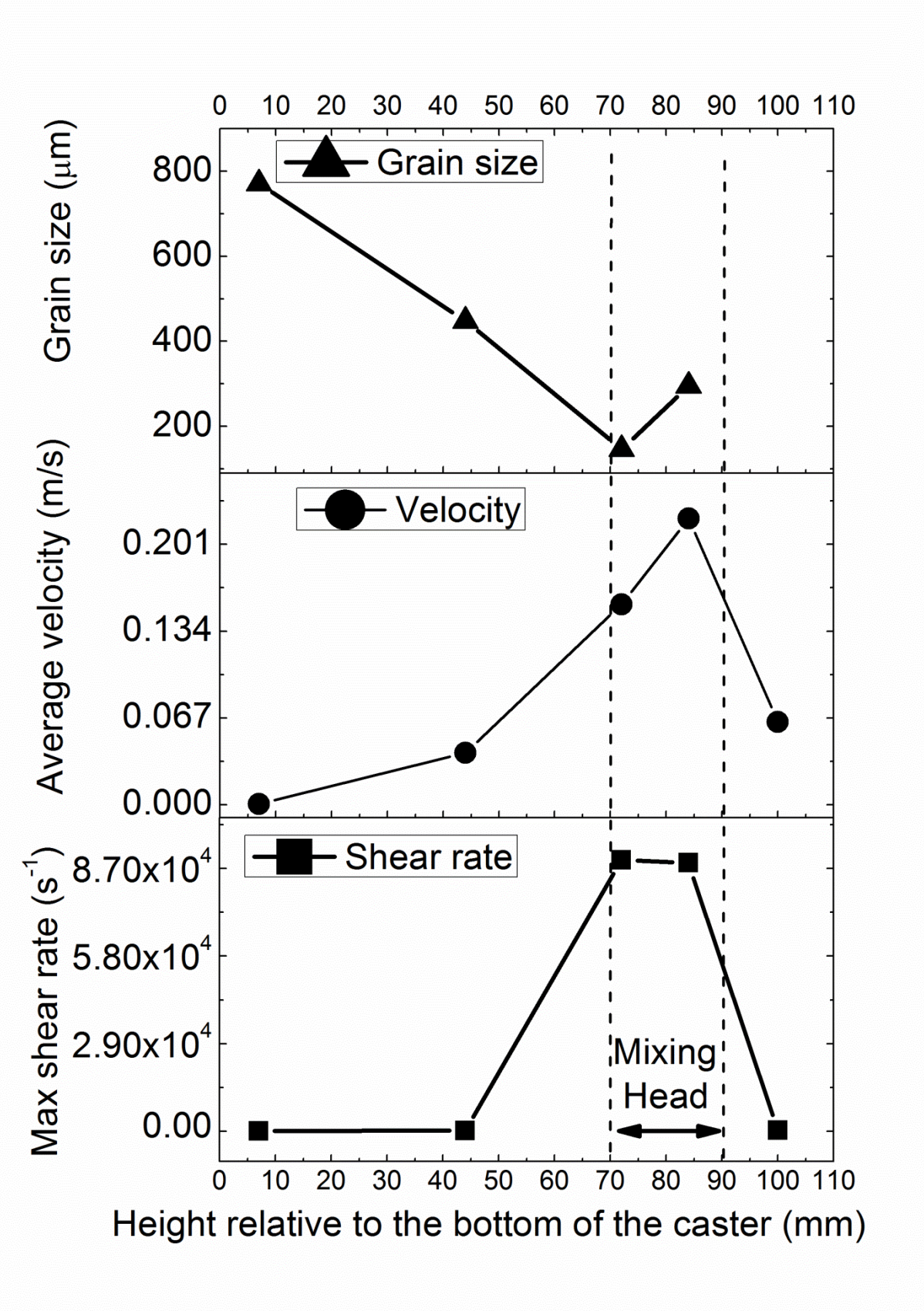


Fig.15. Variation of grain size, area averaged vertical component of melt velocity, and maximum characteristic shear rate, and through the height of the caster.

We can find a clear link between the variation of these three different parameters along the height. In the close vicinity of the mixing head, between a height of 70 mm and 90 mm, there is a very high level of shear rate and vertical component of melt velocity. Because the vertical component of melt velocity characterises the efficiency of the redistribution of the liquid metal from the depth of the caster into the mixing head, this result means that the liquid metal in this range of the depth of the caster is very quickly redistributed through the mixing head where it is dramatically sheared. The resultant vast fine and uniformly distributed oxide particles can act as potent nuclei that dramatically improve the nucleation of equiaxed dendrites inside this region. The dramatic event of nucleation of equiaxed dendrite can trigger the columnar to equiaxed transition (CET) [34], which leads to the small size equiaxed dendrites as shown in Fig.14 (a,b) and Fig.15. Below the fine equiaxed dendrite zone, as shown in Fig.14 and 15, the level of shear rate and vertical component of melt velocity are relatively low. Particularly, the level of shear rate is negligible. This means that the liquid metal is not effectively sheared in this region, and it has very little chance to be redistributed into the mixing head and get sheared either. Therefore there are not enough fine and uniformly distributed oxide particles which can result in significant nucleation of equiaxed dendrites, in this region. The columnar growth of dendrites in this region is dominant, due to the chilling effect by the bottom of the caster. Above the zone of fine equiaxed dendrite, there is a second zone of coarse equiaxed dendrite. Firstly, the sequence of solidification of the billet is from the bottom towards the top. Because CET already occurs in the zone of fine equiaxed dendrites, the solidification has to proceed in the form of equiaxed dendrite from here upwards. Secondly, in this second zone of coarse equiaxed dendrites, the level of shear rate and vertical component of melt velocity is relatively low. The melt is not effectively sheared in this zone and it has very little chance to be redistributed into the mixing head and get effectively sheared either, which can be also found in the localized recirculation of melt as shown in the stream line of Fig.9. Therefore there is a comparatively lower number of oxide particles acting as effective nuclei in this region. This results in the coarse equiaxed microstructure here.

## 4. Discussion and conclusion

By analysing key features of fluid flow during HSP of aluminium alloy, using computer simulation, we found that the distribution of related parameters of the melt flow is highly nonuniform in space. Overall, in the close vicinity of the mixing head, there is relatively high

level of shear rate. Particularly, inside the gap between the rotor and the stator, the level of shear rate is very high, while the level in the far field of the bulk liquid metal is much lower – by a few orders of magnitude. This means that only the melt that can flow through the mixing head is well sheared. The liquid metal is well agitated only in the close vicinity of the mixing head, while the melt deep in the caster is relatively stagnant. Particularly, the melt above the third row of the holes of the stator is found to have little chance flowing into the mixing head. This feature of fluid agitation means that only the melt that is in the close vicinity of the mixing head and below the third row of the holes will be well sheared by the mixer. This conclusion is positively supported, but not directly validated, by the microstructure of the solidified billet of the HSP treated molten alloy.

For full model validation we will have to include computational treatment of heat transfer during the process, grain nucleation and CET formation [34], in order to link nucleation density and potency [35] to grain structure and grain size. This is beyond the scope of the current contribution. However we have already shown in a separate contribution [12] that there is a direct link between shear rate and oxide fragmentation in HSP. So, in theory, a high shear rate should lead to CET and formation of small eqiuaxed grains, as has been shown to be the case in Fig. 15. We have not validated the current model yet, but rather we have highlighted confidence-building experimental evidence.

The computationally predicted features of the HSP of liquid metal with the rotor-stator mixer has a two-fold influence on its application. The positive aspect is that the performance of the mixer is not affected by the geometry (i.e. shape, volume, and relative position) of the container that holds the liquid metal. It makes the design and optimisation of the rotor-stator mixer independent of the environment in which it is going to be applied. For example, the level of shear rate and level of mass flow rate in the close vicinity of the mixing head do not significantly vary when treating either 50 kg or 200 kg of liquid metal. Therefore, the optimised rotor-stator is universal to the varying contexts of application to some extent. However, a negative aspect is that is difficult to shear the liquid metal in the far field of the container effectively. Although the shear rate and mass flow rate in the close vicinity of the mixing head are not affected by changes in container size or shape, when treating a large volume of liquid metal with this rotor-stator mixer a significant part of the bulk liquid not effectively sheared. Due to the specific geometrical feature of the rotor-stator mixer, the inlet for liquid (i.e. the large opening at the bottom of the mixing head) and the outlet (i.e. the

holes at the side of the stator) are very close to one another. This fact results directly in the highly localized strong recirculation of liquid as shown in Fig.9, which is the key reason for the difficulty of agitating the melt deep in the caster.

Overall, HSP of liquid metal with the rotor-stator mixer can shear the liquid metal very well in the close vicinity of the mixing head. If it can be improved in order to effectively agitate a larger volume of liquid metal, it has great potential of application in the industrial scale treatment of molten alloys, for the purpose of purification.

## Acknowledgement

This work is financially supported by the European Commission FP7 project “High shear processing of recycled aluminium scrap for manufacturing high performance aluminium alloys”; Grant Number 603577.

References


1. S. Jones, A. K. Prasada Rao, Z. Fan, Melt conditioned direct chill (MC-DC) casting of Al alloys, Trans Indian Inst Met. 66 (2013) 117–121
2. M. Xiaa, A.K. Prasada Raob and Z. Fan, Solidification mechanisms in melt conditioned direct chill (MC-DC) cast AZ31 billets, Materials Science Forum. 765 (2013) 291-295
3. Y. B. Zuo, B. Jiang, Y. Zhang, Z. Fan, Grain refinement of DC cast magnesium alloys with intensive melt shearing, IOP Conf. Series: Materials Science and Engineering 27 (2011) 012043
4. G. Scamans, H. Li and Z. Fan, Melt conditioned casting of aluminium alloys, 13th International Conference on Aluminum Alloys (ICAA13), 2012, 1395-1400
5. H. T. Li, Y. Wang and Z. Fan, Enhanced heterogeneous nucleation on oxides in Al alloys by intensive shearing, IOP Conf. Series: Materials Science and Engineering. 27 (2011) 012047
6. S. Ji, W.Yang, F. Gao, D. Watson, Z. Fan, Effect of iron on the microstructure and mechanical property of Al–Mg–Si–Mn and Al–Mg–Si die cast alloys, Materials Science & Engineering A. 564 (2013) 130–139
7. H. T. Li, S. Ji, Y. Wang, M. Xia and Z. Fan, Effect of intensive melt shearing on the formation of Fe containing intermetallics in LM24 Al-alloy, IOP Conf. Series: Materials Science and Engineering. 27 (2011) 012075
8. W. Yang, S. Ji, X. Zhou, I. Stone, G. Scamans, G. E. Thompson, and Z. Fan, Heterogeneous nucleation of α-Al grain on primary α-AlFeMnSi intermetallic investigated using 3D SEM Ultramicrotomy and HRTEM, Metallurgical and Materials transactions A. 45 (2014) 3971
9. Z. Fan, Y. Wang, Z. F. Zhang, M. Xia, H. T. Li, J. Xu, L. Granasy and G. M Scamans, Shear enhanced heterogeneous nucleation in some Mg- and Al-alloys, International Journal of Cast Metals Research. 22 (2009) pp 1-5
10. R. Haghayegi, L. Nastac, On microstructural refinement of an AA7449 aluminium alloy through shearing above liquidus temperature, Materials Letters.65 (2011) 3230-3233
11. X. Fang, G. Shao, Y.Q. Liu, Z. Fan, Effects of intensive forced melt convection on the mechanical properties of Fe-containing Al-Si based alloys, Materials Science and Engineering A. 445–446 (2007) 65–72

12. M. Tong, S. Jagarlapudi, J. Patel, I. Stone, Z. Fan, David J. Browne, Computational prediction of the refinement of oxide agglomerates in a physical conditioning process for molten aluminium alloy, IOP Conference Series: Materials Science and Engineering. 84 (2015), 012092.
13. X. Dong, X. Huang, L. Liu, L. He, P. Li, A liquid aluminium alloy electromagnetic transport process for high pressure die casting, Journal of Materials Processing Technology. 234 (2016) 217–227
14. L. Wu, J. Cheon, D. V. Kiran, S. Na, CFD simulations of GMA welding of horizontal fillet joints based on coordinate rotation of arc models, Journal of Materials Processing Technology. 231 (2016) 221–238
15. A.Kidess, M.Tong, G.Duggan, D.J., Browne, S.Kenjeres, I.Richardson, C.R.Kleijn, An integrated model for the post-solidification shape and grain morphology of fusion welds, International Journal of Heat and Mass Transfer. 85 (2015) 667-678
16. Y. Kwon, J. Zhang and H. Lee, A CFD-based nucleation-growth-removal model for inclusion behaviour in a gas-agitated ladle during molten steel deoxidation, ISIJ International, 48 (2008) 891–900
17. V. D. Felice, I. L. A. Daoud, B. Dussoubs, A. Jardy and J. Bellot, Numerical modelling of inclusion behaviour in a gas-stirred ladle, ISIJ International, 52 (2012) 1273–1280
18. P. Gardin, J.F. Domgin, M. Simonnet, J. Lehmann, Modeling of inclusion evolution in a steel ladle or in RH degasser, Revue de Metallurgie, 105 (2008) 84-91
19. J. Cheng, C. Yang, Z. Mao, and C. Zhao, CFD modelling of nucleation, growth, aggregation, and breakage in continuous precipitation of barium sulfate in a stirred tank, Ind. Eng. Chem. Res. 48 (2009) 6992–7003
20. Z. Fan, B. Jiang, Y. Zuo, Apparatus and method for liquid metals treatment, Patent US20130228045, 2013
21. A. T. Utomoa, M. Bakerb, A. W. Pacek, Flow pattern, periodicity and energy dissipation in a batch rotor–stator mixer, Chemical Engineering Research and Design. 86 (2008) 1397–1409
22. A. Utomoa, M. Bakerb, A.W. Pacek, The effect of stator geometry on the flow pattern and energy dissipation rate in a rotor–stator mixer, Chemical Engineering Research and Design. 87 (2009) 533–542

23. S. Jones, A. K. Prasada Rao, J. B. Patel, G. M. Scamans and Z. Fan, Microstructural evolution in intensive melt sheared direct chill cast al-alloys, in ICAA13: 13th International Conference on Aluminum Alloys (eds H. Weiland, A. D. Rollett and W. A. Cassada), John Wiley & Sons, Inc., Hoboken, NJ, USA, 2012, 91-96.
24. T. H. Shih, W. W. Liou, A. Shabbir, Z. Yang, and J. Zhu, A new eddy-viscosity model for high reynolds number turbulent flows – model development and validation, Computers Fluids. 24 (1995) 227–238
25. ANSYS® Academic Research, Release 17.0, Help System, "Turbulence", ANSYS, Inc.
26. C.W. Hirt, B. D. Nichols, Volume of fluid (VOF) method for the dynamics of free boundaries, Journal of Computational Physics. 39 (1981) 201–225
27. D. L. Youngs, Time-Dependent Multi-Material Flow with Large Fluid Distortion, Numerical Methods for Fluid Dynamics, K. W. Morton and M. J. Baines, editors, Academic Press. 1982.
28. J. U. Brackbill, D. B. Kothe, and C. Zemach, A Continuum Method for Modeling Surface Tension, J. Comput. Phys. 100 (1992) 335–354.
29. ANSYS® Academic Research, Release 16.2, Help System, Theory Guide, ANSYS, Inc.
30. S. V. Patanker, D. B. Spalding, A calculation procedure for heat, mass and momentum transfer in three-dimensional parabolic flows, International Journal of Heat and Mass Transfer. 15 (1972) 1787-1806
31. Y. Yitao, Z. Henghua and S. Guangjie, Application of computer simulation in developing automotive parts of Al alloy by using semi-solid die cast process, Solid State Phenomena. 116-117 (2006) 630-634
32. Tables of Physical & Chemical Constants. 2.1.2 Barometry. Kaye & Laby Online. Version 1.1 (2008)
33. J. Schmitz, J. Brillo, I. Egry, R. Schmid-Fetzer, Surface tension of liquid Al-Cu binary alloys, Int. J Mat. Res. 100 (2009) 1529-1535
34. W.U.Mirihanage, H. J Dai, H.B.Dong, D.J. Browne, Computational modelling of columnar to equiaxed transition in alloy solidification, Advanced Engineering Materials. 15 (2013) 216-229
35. A.G. Murphy, W.U. Mirihanage, D.J. Browne, R.H. Mathiesen, R.H., Equiaxed dendritic solidification and grain refiner potency characterised through in situ X-radiography, Acta Materialia. 95 (2015) 83-89